



HAL
open science

Experimental observation of low-frequency interactions at different scales and evidence of transit time oscillations in a Hall thruster: Spectral analysis

Quentin Delavière–Delion, F. Gaboriau, G. Fubiani, L. Garrigues

► To cite this version:

Quentin Delavière–Delion, F. Gaboriau, G. Fubiani, L. Garrigues. Experimental observation of low-frequency interactions at different scales and evidence of transit time oscillations in a Hall thruster: Spectral analysis. *Physics of Plasmas*, 2024, 31 (7), pp.072110. 10.1063/5.0206369 . hal-04657851v2

HAL Id: hal-04657851

<https://hal.science/hal-04657851v2>

Submitted on 31 Jul 2024

HAL is a multi-disciplinary open access archive for the deposit and dissemination of scientific research documents, whether they are published or not. The documents may come from teaching and research institutions in France or abroad, or from public or private research centers.




L'archive ouverte pluridisciplinaire **HAL**, est destinée au dépôt et à la diffusion de documents scientifiques de niveau recherche, publiés ou non, émanant des établissements d'enseignement et de recherche français ou étrangers, des laboratoires publics ou privés.



Distributed under a Creative Commons Attribution - NonCommercial 4.0 International License

RESEARCH ARTICLE | JULY 19 2024

Experimental observation of low-frequency interactions at different scales and evidence of transit time oscillations in a Hall thruster: Spectral analysis

Q. Delavière—Delion ; F. Gaboriau ; G. Fubiani ; L. Garrigues 



Phys. Plasmas 31, 072110 (2024)

<https://doi.org/10.1063/5.0206369>



25 July 2024 17:59:27



Physics of Plasmas

Publish open access for free

[Learn More](#)



Experimental observation of low-frequency interactions at different scales and evidence of transit time oscillations in a Hall thruster: Spectral analysis

Cite as: Phys. Plasmas **31**, 072110 (2024); doi: 10.1063/5.0206369

Submitted: 1 March 2024 · Accepted: 13 June 2024 ·

Published Online: 19 July 2024



View Online



Export Citation



CrossMark

Q. Delavière–Delion,^{a)} F. Gaboriau, G. Fubiani, and L. Garrigues

AFFILIATIONS

LAPLACE, Université Paul Sabatier, CNRS, INPT, 118 Route de Narbonne, 31062 Toulouse, France

^{a)} Author to whom correspondence should be addressed: quentin.delaviere@laplace.univ-tlse.fr

ABSTRACT

Hall thrusters are $E \times B$ plasma devices characterised by a large azimuthal electron current, which is involved in the formation of a wide variety of instabilities on different frequency scales (from kilohertz to gigahertz) and propagating in different directions. We have focused on a limited number of low-frequency instabilities that could be experimentally observed, such as breathing mode (BM) and ion transit time oscillations (ITTO). There are still gray areas in the understanding of the mechanisms behind these instabilities, which are often described individually, without considering an eventual exchange of information between the different types of instability. A wavelet time-frequency study of the plasma revealed the coexistence and interdependence of distinct instabilities. We suspect a possible interaction between the breathing mode and higher-frequency oscillations leading to ITTOs: it was shown that a transition occurred when the frequency of one of the BM harmonics became a multiple of the frequency of the higher-frequency oscillations. This was also accompanied by a deformation of the ion energy distribution functions.

© 2024 Author(s). All article content, except where otherwise noted, is licensed under a Creative Commons Attribution-NonCommercial 4.0 International (CC BY-NC) license (<https://creativecommons.org/licenses/by-nc/4.0/>). <https://doi.org/10.1063/5.0206369>

NOMENCLATURE

B	Magnetic field
BM	Breathing mode
E	Electric field
ECDI	Electron cyclotron drift instability
FFT	Fast Fourier transform
HT	Hall thruster
I_d	Discharge current
I_{RPA}	Ion current collected by the RPA
ISP	Specific impulse
ITTO	Ions transit time oscillations
IDF	Ion distribution function
L_c	The characteristic dimension of the channel
LIF	Laser induced fluorescence
MCC	Monte-Carlo collisions
PSD	Power spectral density
PIC	Particles in cell

RF	Radio-frequency
RPA	Retarding potential analyser
RS	Rotating spokes
U_d	Discharge voltage
V_{cg}	Potential of the cathode in reference to the ground
WT	Wavelet transform
\bar{X}	Mean value of signal X

Greek symbols

ε_i	Ionization cost
ρ_α	Larmor radius of an α particle (ion or electron)
ϕ_{RPA}	RPA filtering potential

I. INTRODUCTION

Invented between the 1960s and 1970s in the USSR by Morozov and his colleagues,¹ Hall current thrusters, commonly known as Hall thrusters or SPT (stationary plasma thruster), are a type of electric

propulsion system for spacecraft. The Hall thruster is now the main type of propulsion system used on geostationary satellites² and the use of electric propulsion systems is set to become even more prevalent due to the ongoing trend toward complete electrification of propulsion and attitude control systems. Although their thrust is lower than chemical thrusters, their ISP (proportional to the exhaust velocity) is much higher.^{3,4}

A. Operation of a Hall thruster

A Hall thruster is made up of several components, consisting of the thruster block itself and an emissive cathode. The thruster block consists of a magnetic circuit, a gas injection, and uniformization system, along with an anode. The propellant gas is injected through the anode, at the bottom of an annular channel, the walls of which are made of a dielectric material. The role of the cathode is to supply electrons to the thruster, to initiate and maintain the discharge, and to neutralize the extracted ion beam to keep the plasma electrically neutral. The emissive element of the cathode made of LaB₆ is heated close to 1600 °C by the Joule effect, thanks to an electric current flowing in a resistive element. The emissive material then releases electrons into a cavity in which some of the propellant gas has been rerouted. It is additionally subjected to an electric field, which greatly increases the extraction of electrons. The extracted electrons then collide with the gas atoms, ionizing them. This primary plasma then serves as the electron source for the propellant.

The principle of operation of a HT is relatively simple: a DC voltage of a few hundred volts is applied between the cathode and the anode, and a magnetic field of a few tens of mT, mainly radial, is imposed throughout the channel. The intensity of the magnetic field is chosen to trap only the electrons and not the ions, which results in $\rho_e \ll L_c \ll \rho_i$ where ρ_α is the Larmor radius of an α particle and L_c is the characteristic dimension of the channel.

In a HT, the plasma is created by ionization via electron impacts: some electrons emitted by the cathode enter the channel through its exhaust and are accelerated as they travel up the electric field toward the anode. On their way, they pass through an area with a strong magnetic field that confines them. At the same time, the propellant atoms (usually xenon or krypton) are injected homogeneously from the bottom of the channel and diffuse upwards along it. When they cross the magnetic barrier, they collide with the electrons trapped in the magnetic field.

To ensure an efficient ionization, it is necessary for the propellant atoms to collide with sufficiently energetic electrons. However, to initiate and maintain the discharge, many ionization reactions and, therefore, collisions are necessary. This is why the use of a magnetic field is justified: as the electrons are trapped in the magnetic barrier, their residence time is considerably increased, which significantly increases the probability of ionizing collisions. As a result, this type of device is one of the most effective for ionizing a gas, achieving ionization rates of over 80% assuming that only singly ionized ions are created.

When ionization occurs, an electron–ion pair is created. The electron remains trapped by the magnetic field and diffuses toward the anode through collisions and instabilities. Ions are immediately extracted and accelerated by the electric field, which generates the thrust or it is lost on the dielectric surface of the channel, which contributes to the erosion of the channel.⁵ Finally, the ion beam is neutralized by electrons coming from the cathode.

We note that the operation of a HT requires an electric field and a magnetic field perpendicular to each other. This configuration generates a strong electron drift current in the direction of the $\mathbf{E} \times \mathbf{B}$ product. To avoid the loss of electrons at the walls (and the associated Hall effect), the thruster designers came up with the idea of closing the channel in on itself by giving it an annular shape,¹ thus closing the azimuthal drift of the electron current. This configuration is known as a closed drift configuration. The combination of electric and magnetic fields, together with the strong azimuthal electron current and any inhomogeneities in the plasma or system, creates a source of energy that leads to the development of various instabilities.

B. Instabilities in a Hall thruster

Low-pressure cross-field plasma sources, including HT, produce a wide variety of instabilities that can lead to regular⁶ or transient⁷ oscillating phenomena or lead to turbulence.^{8,9} It has been experimentally observed that these instabilities cover a wide range of frequencies, from a few Hz to several GHz, for wavelengths ranging from a few cm to less than one mm. They are also capable of propagating in both axial and azimuthal directions.

Studied experimentally and theoretically over decades, and more recently using numerical models, there remain many gray areas as to the exact properties and nature of certain instabilities. In addition, to avoid excessive complexity, the most complete theoretical models only look at one instability at a time, ignoring the possible couplings and feedback loops between the different plasma instabilities, and the interactions that may occur between phenomena on different scales. However, understanding the complex dynamics of these instabilities in time and space is a key point in solving the electron transport problem through a magnetic barrier. In this article, we will focus only on low-frequency oscillations (<MHz).

1. Axial instabilities

We can distinguish two main categories of oscillations propagating in the axial direction that can coexist despite being at different frequencies. The physical mechanisms governing their behavior are also different.

a. The breathing mode (BM). The first instabilities take the form of oscillations with long periods and relatively high amplitudes on the discharge current and also on the overall luminosity of the plasma.¹⁰ Their frequency range is from a few kilohertz to a few tens of kilohertz. They were discovered after the invention of the Hall thruster¹ and have regularly been observed since in Refs. 10–18. These oscillations are strongly dependent on the shape and intensity of the magnetic field,^{19,20} on the applied discharge voltage, the gas flow rate, and the material making up the channel walls.^{1,20} In some cases, these oscillations are strong enough to extinguish the discharge or damage the electrical power unit. The characteristic shape of the discharge current, with its strong oscillations, is not dissimilar to a predator-prey model (Lotka–Volterra). Different studies that explored this similarity²¹ have shown that the oscillation frequency was related to the gas flow and the ionization rate in the HT channel. More developed models have been proposed to justify the observed behavior. We might mention in particular, the 1D hybrid model developed by Garrigues and Boeuf²² from which the following explanation is given: the triggering of oscillations is caused by the fact that in a HT, the ionization process can be so

efficient that all the neutrals present in the ionization zone are ionized faster than the flow of gas can replace them; thus, the ionization front moves deeper into the channel, toward the anode. This leads to a reduction in ionization efficiency (the magnetic trapping of electrons is less effective as we move closer to the anode), which can lead to a quasi-extinction of the discharge, allowing the neutrals to repopulate the channel (i.e., the ionization region). As the ionization restarts, the neutrals are again depleted and so on. The alternating nature of this instability is the reason behind its name “breathing mode” (by analogy of the inhalation of air/neutral gas during BM’s phase 1 and the consumption and expulsion of combustion products/ionization and extraction of ions during phase 2). More sophisticated models were then developed,^{23,24} but it remains difficult to simulate/predict the properties of BM due to the different mechanisms involved being interdependent.

b. The ion transit time oscillations (ITTO). Although BM-type oscillations have already been studied extensively, relatively few are actually complete, in particular experimental studies of instabilities occurring at frequencies between a few tens and a few hundreds of kilohertz. These frequencies correspond to the inverse of the time of flight required for the ions to cross the acceleration zone, hence the name ion transit time oscillations given to oscillations within this frequency range. These oscillations leave their mark on the discharge current, where they generally coexist with other oscillations, such as the BM, but they are usually less prominent. Similar oscillations can be found in certain fluid,^{25,26} hybrids,²⁷ and PIC-MCC models.²⁸ Based on the descriptions provided by the literature, we can say that one of the major characteristics of ITTOs is the presence of oscillations in the potential distribution in the thruster channel and also in the first few cm of the plume. These oscillations in the electric field have a significant impact on the acceleration of the ions: during one part of the oscillation, a fraction of the ions surf on the electric field wave⁶ and, therefore, always see the maximum electric field, which gives them an additional acceleration, sometimes bringing their kinetic energy to more than that provided by the applied potential energy. During the other half of the oscillation, some of the ions are accelerated less efficiently and gain less speed because they do not see the full potential difference. These changes in the speed of the ions distort the ion energy distribution function (IDF), disrupt the ion currents (and consequently also the discharge current, which is the sum of the ion and electron currents), and modify the ion density profile over time (bunch emission due to the segregation of ions as a function of their speed), which all have a feedback effect on the potential distribution. However, there are points of divergence between more recent studies and older Soviet ones carried out in the early days of HT. Contemporary models contradict the hypotheses put forward at the time: ITTOs were described as quarter-wave resonators that would impact electron movements.²⁹ It should be remembered that on early HTs, the magnetic barrier was positioned deeper in the channel than in modern HTs. It should also be noted that the configuration of the ID-Hall 2 thruster is halfway between these two configurations.

2. Azimuthal instabilities

Azimuthally propagating modes have been observed in the HT channel and more generally in $E \times B$ devices. These include ECDI/EDI: electron drift instabilities, in the megahertz range^{30,31} and rotating

spokes (RS). RS manifest themselves by an azimuthal displacement of coherent structures resulting in variations in luminosity, potential, and discharge current at frequencies of the order of a few kilohertz to a few tens of kilohertz.^{32–35} Their azimuthal displacement speed is an order of magnitude lower than the speed of the $E \times B$ drift current.³⁴ In many experimental studies, the RS are observed together with other instabilities, such as the BM.³⁶ It has recently been shown that the BM and RS can be interdependent, leading to axial-azimuthal coupling of the RS, which then describes a helical movement within a BM cycle.³⁶ The combination of fast imaging and the use of a segmented anode has highlighted the fact that almost 50% of the total discharge current flows through the luminous structures of the RS, even though the RS occupies only about 1/4 of the channel surface area.³⁴

In this article, we look into the signatures of these oscillations on different types of signals. First, in Secs. III A 1 and III A 2, we identify different oscillation regimes as a function of parameters, such as discharge voltage and gas flow rate, and discuss the characteristics of these different oscillations identified on the time series of the discharge current and a capacitive signal. In each of these oscillation regimes, the discharge, ion, and average electron currents are also studied, as well as the energy cost of extracting an ion. Then, in Sec. III A 3, we discuss the characteristics of the mean ion distribution functions, pointing out, in particular, the existence of an asymmetry of the IDF in one of the oscillation regimes identified previously, in which a doubling of the amplitude of the discharge current oscillation was observed. Finally, in Sec. III B, we present the results of using a time-frequency analysis technique called the wavelet transform. This diagnostic is used to highlight the links between the different oscillations taking place at different times and/or at different frequencies. Section III B 1 is devoted to a brief introduction to the method itself, while Sec. III B 2 shows the application of the method to the time series of the discharge current and a capacitive signal picked up outside the vacuum vessel. Finally, Sec. III B 3 describes the oscillations detected in the ion current, the temporality of which is revealed by wavelet transforms.

The detection of different phenomena moving in the azimuthal direction was carried out using a segmented anode composed of three electrically independent segments all recording the discharge current. In this paper, we have only qualitatively described the zones where RS could exist and whether their presence might have an impact on the rest of the discharge.

II. EXPERIMENTAL SET-UP

A. The ID-Hall 2 thruster

The results presented in this paper were obtained by using the experimental ID-Hall 2 thruster (inductive double stage Hall thruster, version 2). Figure 1 shows a schematic view of the ID-Hall 2 thruster, its magnetic field lines and their strength. This is a low-power thruster, operating between 80 and 400 W. The ID-Hall 2 thruster, like its predecessor ID-Hall, was designed and built by the LAPLACE laboratory in Toulouse, with the support of the French space agency CNES. The characteristics of the ID-Hall experimental thruster and its plasma have already been explored and made public in the following publications.^{7,10,15,36,37}

The idea behind using a second ionization source is to facilitate the ionization of propellants that are more difficult to ionize, such as argon or krypton, but that are more abundant and, therefore, less

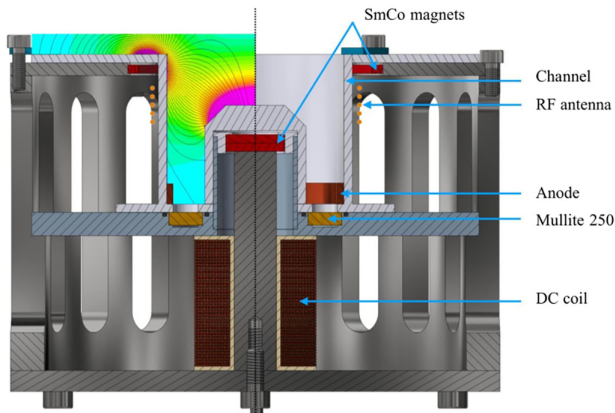


FIG. 1. Schematic view of ID-Hall 2 thruster and associated magnetic field lines. The colormap indicates the norm of the magnetic field, from cyan for the lowest B values (<2.5 mT) to dark pink for the highest B values (>4.75 mT). This figure has been modified from Ref. 10.

expensive. It has also been shown that the addition of RF power can moderate certain instabilities, such as the breathing mode.¹⁵ ID-Hall 2 incorporates feedback from its predecessor with the aim of improving ion confinement close to the ICP source, in order to reduce the ionization cost and increase ion extraction efficiency. (The RF source consists of a coil of a few copper turns surrounding the outer wall of the channel. In Fig. 1, these elements are represented by the orange dots.) To this aim, it was decided to move the RF ionization zone closer to the accelerating magnetic field barrier. This meant that the magnetic configuration had to be modified: the magnetic cusp was removed, leaving only a single magnetic barrier, and the anode was placed into a zone with almost zero magnetic field. With this setup, the magnetic field adopts a configuration close to that of cylindrical Hall thrusters.^{38,39} The bending of the field lines enables the magnetic barrier to cover the ICP ionization

zone and brings it closer to the acceleration zone. The magnetic field is generated by SmCo permanent magnets. The DC coil intended for varying the intensity of the magnetic field is not powered here.

In this article, we will only consider the case of the thruster operating in the single-stage mode, i.e., without using the RF coil.

B. The test bench

The ID-Hall 2 thruster is mounted on one of the inside faces of a 1 m long and 0.5 m wide cylindrical vacuum chamber. The chamber is equipped with a pumping system consisting of three turbo-molecular pumps connected to two primary pallet pumps. The pumping rate of the system is 4200 l/s.¹⁶ Without gas injection, the lowest achievable pressure in the chamber is of the order of 10^{-6} mbar (10^{-4} Pa). With gas injection, the pumping system maintains a pressure of around 10^{-4} mbar (10^{-2} Pa). The pressure inside the chamber is measured using an Adixen ACC 2009 gauge.

In operation, the thruster uses a MIREA-type emissive cathode with LaB₆.⁴⁰ The cathode is heated by the Joule effect by applying an electric current of 14.5 A to the resistive element (the helical wire in the cathode in Fig. 2) for a power dissipation of 240 W. To preserve the cathode and increase the lifetime of the heating filament, heating/cooling of the cathode is carried out by incrementally increasing/decreasing the current (0.5 A) sent through the filament. The procedure takes around 15 min. The cathode gas flow rate was maintained at 0.25 mg/s of xenon. The thruster gas flow was varied over a range from 0.4 to 1.2 mg/s of xenon. Flow rates were controlled by Brooks mass flow controller 5850TR and Bronkhorst mass flow meter EL-FLOW.

To be more representative of space flight conditions and as we see in Fig. 2 with the blue wires, the thruster’s electrical system, which includes the anode, cathode, keeper (ignitor), and their respective power supplies, is kept floating in relation to the ground (here, the metal housing of the vacuum vessel), this potential is called the cathode common. The discharge voltage is supplied by a Delta Electronika SM-400-AR-8 power supply.

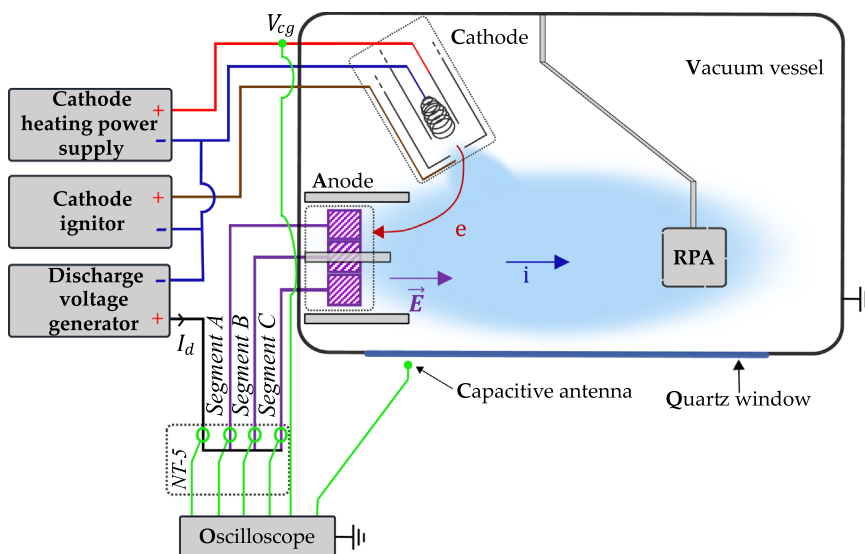


FIG. 2. Thruster electrical circuit schematic diagram.

C. Diagnostics

1. Measurement of time varying properties

The discharge current is measured using a Bell-NT5 magneto-resistive sensor. This sensor is positioned in the electrical circuit between the anode and the discharge voltage generator (green circles in Fig. 2). The discharge current flows through the sensor, which returns a voltage proportional to the discharge current. This voltage is then acquired directly by a digital oscilloscope with an input impedance of $1\text{ M}\Omega$. The oscilloscope used throughout the study is an Agilent Infiniium MSO9254A. The following quantities are also measured directly on the oscilloscope:

- The potential difference between the cathode and the ground is noted as V_{cg} (measured on the green point in Fig. 2).
- The voltage on a capacitive antenna is placed outside the chamber, against the side quartz window of the vessel. This antenna records all the electromagnetic and potential disturbances induced by the plasma, without undergoing any charge recombination on its surface. The probe was moved along the 42 cm of the quartz window and no significant change in the shape of the signals was observed between the different locations, the amplitude that decreased as the antenna was moved further from the thruster. Below about 10 MHz, the signals measured on two antennas placed at the extremities of the window remained coherent and no significant phase shift was measured.

2. Faraday probe

A Faraday probe is an instrument commonly used to measure the ion flow.⁴¹ When mounted on a rotating arm, it can also be used to estimate the divergence of the ion beam. By knowing the collection surface of the probe, it is possible to determine the total ion current I_i extracted from the thruster. Then, by subtracting the ion current to the discharge current I_d , we determine the electron current I_e coming from the cathode. The Faraday probe measurements were carried out using a two-sided flat probe with guard rings. The probe and the protocol are described in Refs. 10 and 16, with the exception that the measurement points were recorded manually using a multimeter. It should be noted that the measurements were carried out at different angles to the thruster axis, to obtain the angular distribution of the ion current. To determine the total ion current, assuming axisymmetry of the discharge, a hemispherical integration is performed.

3. IDF averaged over time

To measure the mean distribution functions of the ions in the thruster plume, we used an RPA (retarding potential analyzer) with four grids. It was designed and built by the GREMI laboratory in Orléans in 1998; design details are available here.⁴²

The aim of this instrument is to filter ions according to their kinetic energies, so that only selected ions are detected and contribute to the measured current. The first grid is called the screening grid and is used to isolate the plasma from the instrument's own electric field and is left floating. The second grid is the electron repulsion grid. As its name states, its role is to repel the electrons from the plasma, allowing only the ions to pass through. It is polarized negatively at -35 V , corresponding around 5–6 times the electron temperature in the

plume. The third grid is the ion discrimination/filtering grid. It creates the potential barrier through which only sufficiently energetic ions can pass and, therefore, contribute to the collected current. The last grid is also an electron repulsion grid. Its role is to send back the secondary electrons emitted by the collector due to ion bombardment. It is polarized at -40 V . Via recombination, the ions impacting the collector induce a current $I_{RPA}(\phi_{RPA})$, which can be measured using an oscilloscope, and which is proportional to the flow of ions with an energy greater than the minimum energy ϕ_{RPA} required to cross the potential barrier. We note f the ion velocity distribution function (IVDF),

$$f(\phi_{RPA}) \propto -\frac{dI_{RPA}(\phi_{RPA})}{d\phi_{RPA}}. \quad (1)$$

It is necessary to apply a correction to compensate effects of the potential difference between the electrical system of the thruster, which is free-floating, and the RPA, which is referenced to the ground. To do this, we subtract $q_i V_{cg}$ from the measured ion energy, with $q_i = 1$ (only singly charge ions).

Before calculating the IDF, it is essential to filter the measured signals to reduce the noise, which would then be exacerbated by the calculation of the derivative shown in Eq. (1). To accomplish this, the Savitzky–Golay (SG) algorithm is used.^{43,44} The obtained IDFs are then also processed by the SG algorithm for a final filtering.

III. RESULTS AND DISCUSSION

During the experimental characterization of the ID-Hall 2 thruster, numerous oscillations were observed. The results presented here focus on the single-stage operation of the thruster, i.e., without RF power injection, like a conventional cylindrical Hall thruster.

A. Oscillation regimes

Since ID Hall-2 has a magnetic field imposed by permanent magnets, the only parameters that can be modified to study the plasma behavior are the thruster gas flow rate and the discharge voltage applied between the anode and cathode. The gas used in single-stage mode is exclusively 99.99% pure xenon. The gas flow rate and the power dissipated in the cathode are fixed and kept constant for all experiments.

1. Current evolutions

Figure 3 shows the current–voltage characteristic of the thruster for a gas flow rate fixed at 0.9 mg/s . It can be seen that the average discharge current follows a classic pattern already observed as the discharge voltage increases.²⁰ At low voltage, the mean value of the discharge current \bar{I}_d quickly increases with the discharge voltage U_d , rising from 0.6 to 1.0 A for a 70 V increase. This increase can be explained by the fact that we are in a zone where the ionization efficiency rises sharply with the addition of electrical energy and, therefore, with the increase in electron energy. The increase in the ionization efficiency was demonstrated experimentally by observing the increase in the total ion current I_i with a Faraday probe in Fig. 4. If we assume that all the ions created are singly-charged, the ionization rate, estimated by calculating the ratio between the ion current and the theoretical maximum ion current if all the gas is ionized once (represented by the dark blue dotted line), rises from 50% to 80%. The measurements, illustrated in Fig. 4(a), were carried out at a gas flow rate of

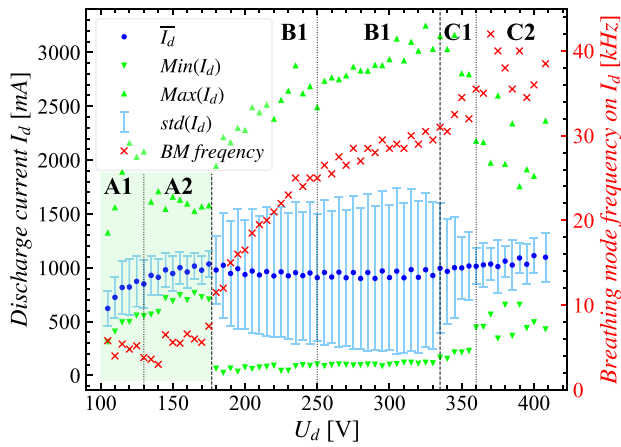


FIG. 3. Thruster characteristics for 0.9 mg/s of xenon. The blue dots represent the mean discharge current, the green triangles mark the extrema of the discharge current (the minimum/maximum for those pointing downward/upward), and the cyan error bars symbolize the standard deviation of the oscillations. In red, on the right-hand axis, the frequency of the main oscillation (breathing mode).

0.6 mg/s. As the discharge characteristics are similar and the evolution of the ion current increases proportionally to the increase in the propellant gas flow rate [blue curve in Fig. 4(b)], we can assume that the results are of the same order of magnitude; for a flow rate of 0.9 mg/s, a measurement was carried out for $U_d = 250$ V and the ionization rate was estimated at 88%. Above 175 V and up to 250 V, the average discharge current inflects and decreases slightly, from 1 to 0.925 A. It then remains constant up to 335 V. In the literature, this zone is known as the plateau zone.²⁰ In this regime, the maximum ionization of the propellant is reached and the ion current is almost unchanged [there is also a plateau on the ion current curve in Fig. 4(a)]. At higher discharge voltages, the discharge current increases due to an increase in the electron current coming from the cathode [red curve in Fig. 4(a)] which can be linked to a change in the electron conductivity in the magnetic barrier. As can be seen in Fig. 5, this change in electron mobility across the barrier also causes a considerable increase in the cost of ionization of a gas atom. This reflects the fact that an increasing proportion of the created ions are lost on the walls, which also increases the secondary electronic emission on the ceramic walls. The electron current I_e is obtained by subtracting the total ion current I_i from the discharge current I_d and the effective ionization energy cost is calculated as follows: $\epsilon_i = U_d I_e / I_i$. Our exploration of the thruster operating range was limited at high voltage by the maximum voltage of the generator (408 V). The lower limit is imposed by the plasma itself: below 105 V, it is no longer possible to maintain a stable discharge. The values of the ion and electron currents measured show that the thruster used in our study can be considered representative of cylindrical thrusters.³⁸

If we now observe the evolution of the discharge current as a function of U_d , we can see that oscillations are always present. In Fig. 3, these current oscillations are represented by the extreme values and standard deviation of the current time series. At low voltage, the oscillations tend to be of low amplitude, although two sub-regimes of oscillation can be distinguished. At very low voltage, the maximum amplitude of the oscillations increases as the voltage U_d increases

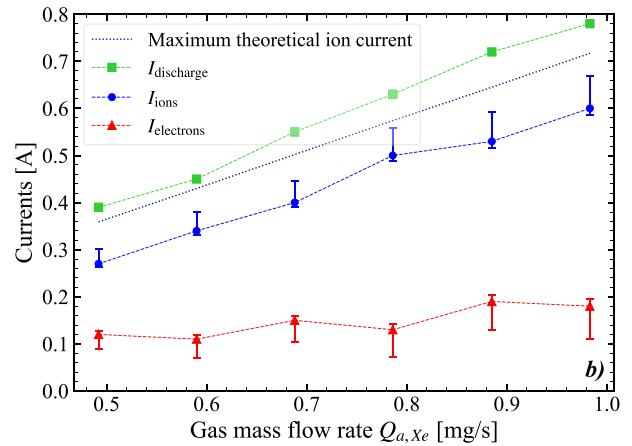
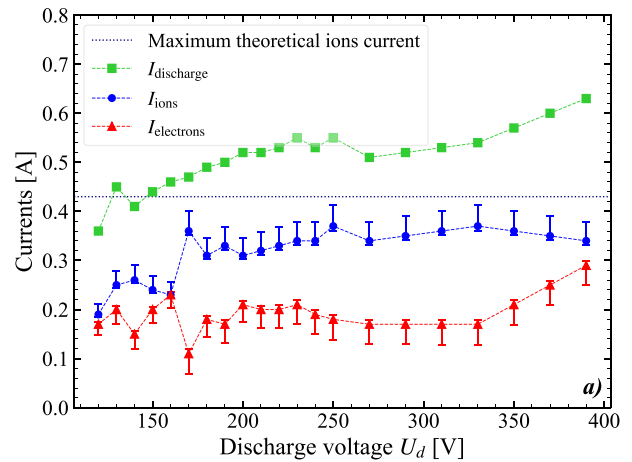


FIG. 4. Average discharge I_d , ions I_i , and electrons I_e currents as a function of the: discharge voltage for 0.6 mg/s of gas injected into the thruster channel: (a) top graph; the gas flow rate injected through the anode for a discharge voltage set at $U_d = 250$ V: (b) bottom graph.

(regime A1), until the oscillations stabilize with smaller amplitudes (regime A2). Figure 6 plots the discharge current over a period of a few oscillations. At very low voltage (110 V in this case), the oscillations are very irregular, with unstable BM oscillations in both frequency and amplitude. We can also see the higher frequency oscillations that are triggered when the current is at its maximum. The frequency instability is also clearly visible on the discharge current spectrogram (Fig. 7), where we can see that the width of the frequency range swept by the BM extends from 3 to 8 kHz. When increasing U_d above 130 V, the BM becomes progressively more regular and increases its oscillation frequency. An example of the current is given in Fig. 6, for $U_d = 150$ V. The intermittent nature and imperfect periodicity of fast oscillations make it difficult to capture their frequency using a FFT, which, nevertheless, gives us a frequency range of between 100 and 200 kHz. In this range of low voltage operation, we observed azimuthal variations in the discharge current at frequencies of the order of tens of kilohertz, which could be assimilated to RS. In Fig. 3, the transparent green area indicates the discharge voltages at which these azimuthal

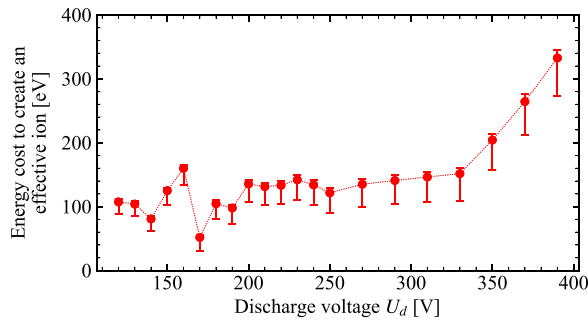


FIG. 5. Evolution of the effective ionization energy cost of a xenon atom as a function of the discharge voltage for a gas flow rate fixed at 0.6 mg/s.

structures were observed. It was also observed that the higher the gas flow rate and the lower the discharge voltage, the greater the probability of observing phenomena moving in the azimuthal direction, and the number of occurrences per BM also increased. We note that these

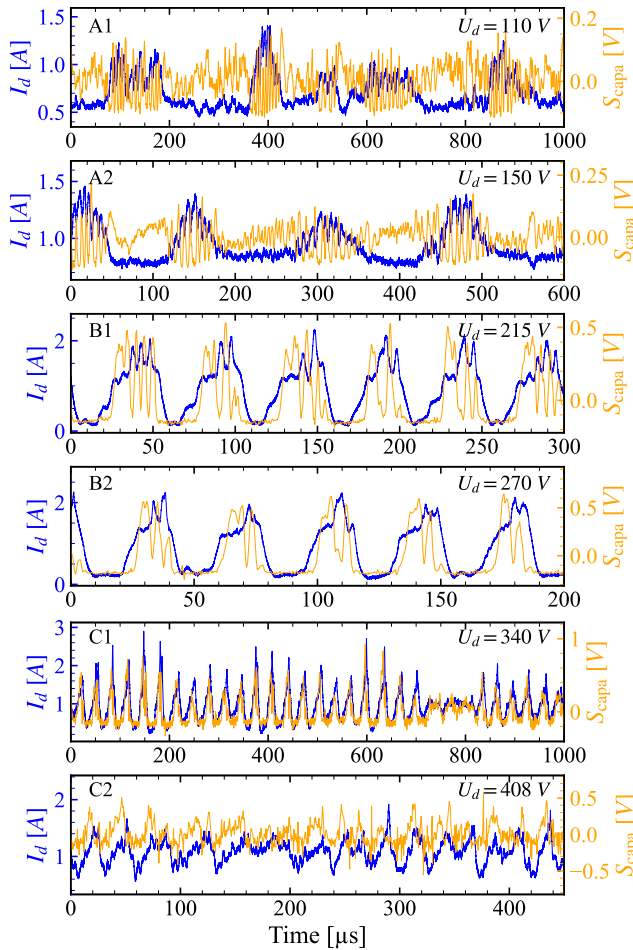


FIG. 6. A few time series in each of the regimes identified in Fig. 3, with in blue, the discharge current and in orange, the voltage of the external capacitive antenna.

oscillations are in addition to the axial oscillations already observed, such as the BM and ITTO, as well as other oscillations at higher frequencies.

When increasing U_d , there are significant changes in the shape, amplitude, and frequency of the oscillations. The amplitude of the oscillations doubles and can exceed 3 A, and the current also passes practically through zero at the minimum of the BM. These oscillations can lead to temporary extinction of the discharge. The spectrogram in Fig. 7 shows that the frequency of the BM increases rapidly for $U_d \in [175-250]$ V (regime B1), before slowing down for $U_d \in [250-335]$ V (regime B2). The frequency range of the fast oscillations remains the same as that identified previously, so the number of fast oscillations per BM cycle decreases as the discharge voltage increases (since the BM period decreases). It can also be seen that for each voltage, the frequency of BM oscillations stabilizes around a central frequency with a small dispersion of merely a few kHz. In addition, the first harmonics of this frequency become much more pronounced, to the point where we can observe an overlap between the frequency domain of fast oscillations and certain harmonics of the BM (between the 4th and the 7th).

If the discharge voltage is increased further, alternations between different oscillation modes can be seen in Figs. 3 and 6. A first transition zone can be defined for $U_d \in [335-360]$ V, where BM oscillations are still present but alternate between high and low amplitude modes, 2.5 and 1 A, respectively (C1 regime). For higher voltages $U_d \geq 360$ (C2 regime), low-amplitude BM oscillations alternate with oscillations of reduced amplitude (0.4 A) and higher frequency (between 150 and 250 kHz), which more closely resemble the rapid oscillations previously found when the discharge current was at its maximum. These changes are associated with a loss of regularity in the oscillations, resulting in a widening of the frequency range, a reduction in the spectral power density and the disappearance of the BM harmonics from the spectrogram.

An analysis of the characteristic in Fig. 3 also reveals a hysteresis phenomenon: alternations can be seen in both the mean current,

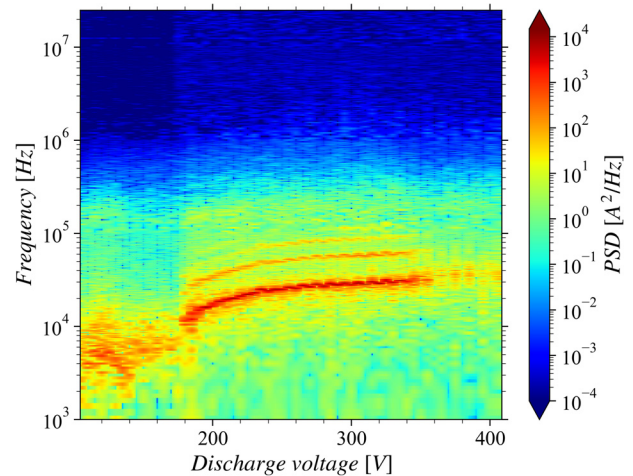


FIG. 7. Spectrogram of low-frequency oscillations in the discharge current of the thruster for 0.9 mg/s of xenon. The time series were measured every 5 V with a sampling frequency of 50 MHz. (To generate this image, a zero-order spline interpolation was performed.)

standard deviation, and in the extreme values reached along with the frequency of BM oscillations. To understand the origin of this phenomenon, we need to take a closer look at the experimental measurement protocol: starting from one operating point of the thruster, the discharge voltage is increased by a 10 V step. Then, once the maximum voltage has been reached, the voltage is shifted by 5 V and decreased again by 10 V, a reversed operation is carried out when the minimum discharge voltage is reached. This procedure shows that the plasma does not behave in the same way when the discharge voltage is raised and lowered. We also note that the plasma requires a few seconds to a few minutes to stabilize after each change in its operating conditions. This difference could be dictated either by the time taken to reach a new thermal equilibrium with the walls⁴⁵ or by a change in the surface state of the ceramics due to their temperature⁴⁶ or to the deposition/spraying of particles, such as ceramic, steel, or/and aluminum in the enclosure, or by all three phenomena at once. This would underline the sensitivity of the BM to secondary electron emissions. In addition, close to the transition discharge voltages, the standard deviation also reflects the proportion of time spent in each of the oscillation modes. Thus, we can see that the transition between two regimes is not well defined and does not occur for a very precise voltage. Instead, we have a hysteresis at the transition point between regimes and, therefore, a shift in the transition discharge voltage depending on the previous state of the plasma. The switch between regimes is, thus, delayed toward the high voltages, respectively, the low voltages (of about twenty volts) when the discharge voltage applied to the plasma is progressively increased (respectively, decreased). This highlights the non-linear nature of the physics governing plasma discharges in HT.

Although the thruster used in our study is very different from the STP-100ML, a striking similarity in terms of frequency distribution with the increase in discharge voltage and in particular, the BM frequency can be observed between our spectrogram and the one shown in Fig. 5 of the article.²¹ This could be attributed to the use of ceramics made from the same material: BN-SiO₂.

Let us now focus on the fast oscillations. Fast oscillations are defined as oscillations whose frequencies are at least one order of magnitude higher than the BM frequency. In the current vs time graphs in Fig. 6, it can be observed that these oscillations are primarily present when the discharge current is at its maximum during a BM oscillation. It is also noticeable that the number of fast oscillations per BM cycle decreases with the increase in U_d . These oscillations have frequencies ranging from a few tens to a few hundreds of kilohertz. For a gas flow rate of 0.9 mg/s, the analysis of the FFTs associated with the discharge current indicates that these fast oscillations cover a relatively wide frequency range, ranging from 30 to 200 kHz for $U_d = 115$ V and from 200 to 500 kHz for $U_d = 315$ V.

In regime A, the frequencies of the fast oscillations do not appear to change significantly when the discharge voltage is modified. Considering that increasing U_d leads to an increase in the BM frequency (i.e., a decrease in its period), this explains why when the discharge voltage is increased, fewer fast oscillations are observed per BM cycle.

In regime B, we see far fewer rapid oscillations per BM cycle, just a few and sometimes just one, with the number of occurrences decreasing with an increasing U_d . Their amplitude distribution also changes: the first oscillations have a very low relative amplitude, whereas the last oscillations appearing during a BM cycle are more

noticeable. The frequency of these oscillations seems to be constrained by the period of the BM, which would exert a forcing effect on these faster oscillations. It is interesting to note that in this regime, the appearance of fast oscillations leads to an increase in the maximum discharge current, sometimes even doubling it. We might, therefore, assume that there is possibly a resonant interaction between the fast oscillations and the BM that could explain this change.

In regime C, if the BM is intermittent, the rapid oscillations never cease. Their frequency dispersion is also narrower, centered around 200 ± 100 kHz.

To sum up, based on what we have observed, we can identify the following regimes: a low-frequency BM oscillation regime for $U_d \in [105-175]$ V (regime A), a high-frequency BM regime for $U_d \in [175-335]$ V (regime B), and an unstable BM regime for $U_d \in [335-408]$ V (regime C). In Fig. 3, these regimes are indicated by thick black dashed lines. The thin black dashed lines represent the boundaries of sub-domains defined by the frequency stability of the discharge. In all these regimes, BM oscillations are present at least transiently and fast oscillations are always present over the BM during the maximum discharge current phase with smaller amplitudes than BM. We will see in Sec. III A 3 that we found exactly the same delimitations for the thruster operating regimes on the ion velocity distribution functions. Plasma oscillations, therefore, have a strong impact on the overall behavior of the ions.

We can add that as U_d increases, an increasing in the luminosity of the plasma and a decreasing in the divergence of the plume is observed. This last observation is in line with the measurement of the divergence of the ion beam by the Faraday probe, where the divergence decreases linearly with the increase in U_d .

2. Characteristics of the discharge current for several gas flow rates

The thruster behavior was tested at different xenon flow rates: 0.4, 0.6, 0.9, and 1.0 mg/s. The different characteristics are shown in Fig. 8, and the evolutions of BM frequencies are shown in Fig. 9. The cases at 0.6, 0.9, and 1.0 mg/s are very similar: they show the same operating modes with variations in amplitude, frequency of BM oscillations, average discharge current, and FDI as a function of flow rate. These values all increase with an increase in the flow rate. The most noticeable differences are found in the locations of the different oscillation modes in terms of discharge voltages, shifting about 20 V lower for the tested flow rate increment. With a flow rate of 0.4 mg/s, the discharge behavior is quite different from that observed for the higher flow rates. At low voltage discharge, BM oscillations are relatively rare, and their distribution over time appears quite random. It is also noticeable that fast oscillations (in the order of hundreds of kilohertz) are present but with very low amplitude (around 50 mA).

To summarize, at a constant discharge voltage, increasing the gas flow rate results in a higher gas density in the thruster channel and, thus, increases the probability of electron neutral collisions. Consequently, ionizing collisions would increase the density of electrons trapped in the magnetic barrier, leading to even more ionizing collisions, and improving the overall degree of plasma ionization. Since it is established that BM is an instability related to global ionization in the channel, this explains why the high BM region can exist at lower voltages when the gas flow rate increases. Assuming there are only singly charged ions, for $U_d = 250$ V, we do, indeed, observe a

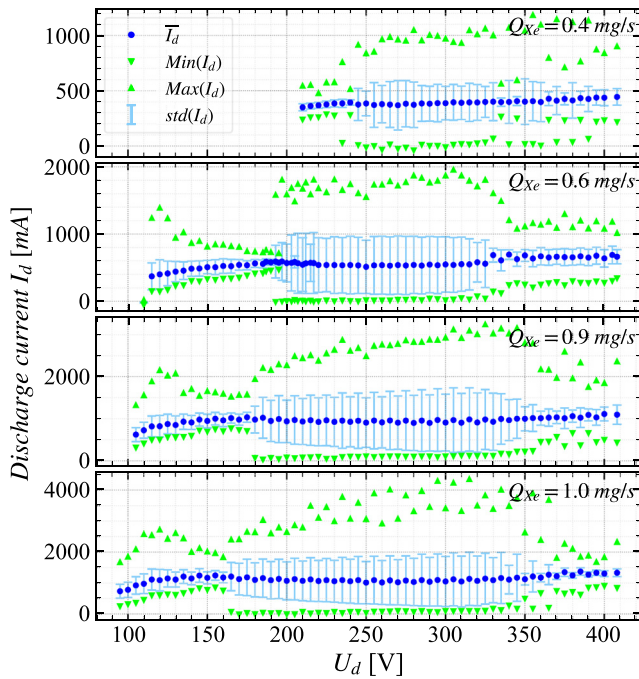


FIG. 8. Thruster characteristics from top to bottom: 0.7, 0.6, 0.9, and 1.0 mg/s of xenon.

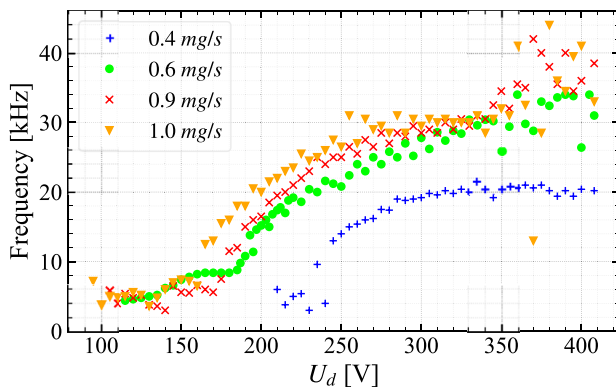


FIG. 9. Central frequencies of the BM for the different flow rates tested.

slight increased ionization rate in Fig. 4(b). As the electron density increases with the gas flow, the mean free path decreases, which could increase the global ionization, explaining the dependence of the BM frequency to the gas flow. It is also noticeable that the frequency spread around the central frequencies of the BM increases with the flow rate. So, the BM oscillations might be destabilized with an increase in the gas flow rate.

3. Time-averaged ion distribution functions

We measured the ion distribution function for different discharge voltages using an RPA. The RPA was positioned in front of the thruster, aligned with the thruster axis, perpendicular to the exit plane

and at 41 ± 1 cm from it. Our results are shown in Fig. 10 for a gas flow rate of 0.9 mg/s.

Two distinct groups of IDF shapes can be observed: a group of relatively symmetrical distributions with a Gaussian appearance, and a group of asymmetrical distributions resembling the sum of two Gaussian functions shifted with respect to each other. We can note that the different plasma oscillation regimes identified as a function of discharge voltage. The behavior of the ions is, therefore, closely linked to the characteristics of the discharge.

The IDFs are relatively symmetrical in the regimes of discharge voltage that correspond to low-amplitude BM oscillations of the discharge current (regime A) and also in the intermittent areas with medium-amplitude BM (regime C). Under the regime of a high-amplitude discharge current (regime B), the distribution functions are asymmetrical and both widen toward high energies, with the gradual appearance of a second peak on the high-energy side, and strongly toward low energies, displacing the initial probability maximum toward the lowest energies. The second peak becomes stronger at the expense of the low-energy peak as the discharge voltage increases until it becomes dominant, causing the less energetic peak to gradually disappear. When the latter has completely disappeared, the transition to regime C is reached.

While symmetrical distributions with a Gaussian shape are common and relatively easy to explain, this is unfortunately not the case for asymmetrical distributions. There are several possible explanations for these differences including the fact that the IDF are not fixed in time but evolves over time in response to plasma oscillations.¹⁶ To confirm this behavior, temporal IDF studies are needed.

B. Time-frequency analysis

While we have been able to identify the main frequency domains of low-frequency oscillations, it is difficult to carry out a more detailed study using a simple FFT. Two intrinsic problems with the properties of the FFT are particularly limiting. First, the FFT transforms an entire time series into a corresponding frequency spectrum, which excludes temporal monitoring of the evolution of the oscillations. Second, by construction, the FFT is very reliable when the phenomenon being

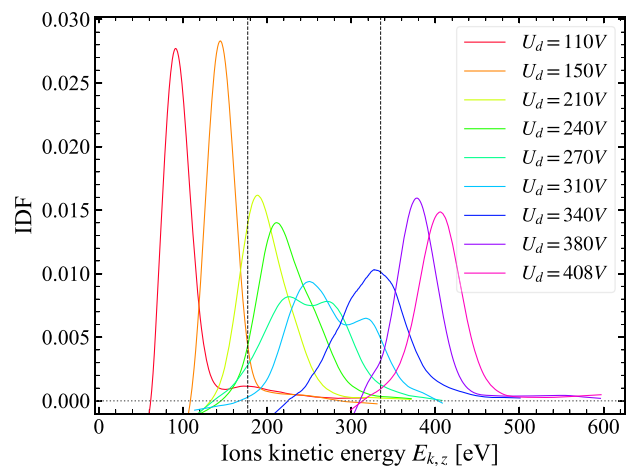


FIG. 10. IDF given for some discharge voltages with a xenon flow rate of 0.9 mg/s.

studied is stationary, which is not the case here. The result is a relative reduction in the weights of the frequencies corresponding to the least regular oscillations and a spectral broadening on the frequency distributions, which makes the frequency bands of the oscillations harder to discern. The FFT, therefore, struggles to effectively capture the different frequencies involved, because the oscillations are neither regular, periodic, nor stable in frequency and are even intermittent, either because some oscillations are triggered selectively or because different oscillation modes alternate along the time series. The use of moving-window Fourier transforms (also known as the short-term Fourier transform) could be a solution if the frequencies of the oscillations studied did not extend over several orders of magnitude, which is our case. Wavelet transforms (WT) are another mathematical tool that offers the best compromise between frequency and time resolution, thanks to the use of a window that is adaptive to the probed frequency. This allows us to probe frequencies over several orders of magnitude, making it possible to study the behavior and interactions of instabilities on several scales at once. There are also diagnostics based on wavelet analysis, which can be used to find a possible direction of propagation of information between the scales of the oscillations.⁴⁷ It should be noted that wavelet transforms are not the only tools suitable for studying the time-frequency behavior of a signal. As an example, we can also mention the Hilbert–Huang transform.¹²

1. Brief introduction to Wavelets

WTs are used relatively frequently in a number of fields, such as the search for instabilities in fusion, the detection of gravitational waves, medicine (the search for warning signs on ECGs), meteorology, and so on. Surprisingly, this type of diagnosis does not seem to be very widespread in the electric propulsion community.^{48–50} In Refs. 48 and 50, they use WT to extract an averaged frequency spectrum from emissive probe measurement and discharge current. In Ref. 49, the authors focus on oscillations from megahertz to a few tens of megahertz, a frequency range that partially overlaps with ours, which mainly probes with frequency ranges going from kHz to a few megahertz.

This article is not intended to provide a detailed explanation of how the WT works. For this purpose, the reader is referred to the documents.^{51–57} Here, we will simply give a general outline. Although similar in appearance, the Gaussian moving window Fourier transform (MWFT) developed by Gabor, sometimes considered to be the first draft of continuous wavelet theory, and WT are fundamentally different. One of the main differences between MWFT and WTs is that the Fourier transform decomposes the signal into a sum of weighted sines waves, where the sine is a localized function in Fourier space, whereas the WT uses a series of dilated/compressed wavelet functions to scan several scales and, thus, best match the corresponding pseudo-frequencies of the functions. These functions, known as mother wavelets, can theoretically be chosen arbitrarily, on condition they satisfy certain rules, such as being an oscillation function with a zero mean, being a summable square function of $L^2(\mathbb{R})$ Hilbert space (be defined in both real and Fourier space).

The wavelet transform $W(\tau, t)$ of a signal $s(t)$ can be expressed using the following equation:

$$W(\chi, \tau) = \frac{1}{\sqrt{\chi}} \sum_{j=0}^{N-1} s(t_j) \phi^* \left[\frac{(t_j - \tau)}{\chi} \right], \quad (2)$$

where χ is a dilation parameter (timescale parameter) and τ is the position parameter (a translation parameter) around which the convolution is performed on a Δt sized window. $W(\chi, \tau)$ is the coefficient of the wavelet transform for a scale factor χ , at time τ . The symbol $*$ designates the complex conjugate and ϕ is a mother wavelet function. Wavelet analysis, therefore, consists of carrying out a local comparison of a signal with a wavelet function, enabling the signal to be zoomed in on at different scales and at all times in the recorded series $s(t_j)$.

The choice of the scale vector on which to expand the wavelet function must be made carefully. If the chosen scale is too low, aliasing may occur if the Shannon–Nyquist condition is not satisfied. Inversely, a too high scale should be avoided as to not make the dilated wavelet function larger than the input signal. In general, scales are inversely proportional to frequencies.

As a mother wavelet function, we have chosen to use the complex Morlet function, which is the result of the convolution between a sinus wave and a Gaussian function (see Fig. 11). The Gaussian shape of the envelope of the Morlet wavelet minimizes the product of the wavelet temporal and frequency resolutions and, therefore, optimizes the accuracy of the results.⁵⁴ This wavelet function has two free coefficients f_0 and β_b ,

$$\phi_{f_0, \beta_b}(t) = \frac{1}{\sqrt{\pi\beta_b}} e^{2i\pi f_0 t} e^{-\frac{t^2}{\beta_b}}. \quad (3)$$

The choice of these coefficients also plays an important role: the optimum value for the central frequency f_0 is 1. Moving away from this value reduces the quality of the time/frequency compromise, increases edge effects, promotes aliasing, and destroys the approximation of the conversion relationship between scales and frequencies. The bandwidth β_b has a direct impact on the balance between frequency and time resolution. It is customary to set it between 3 and 6, and we have empirically set it at 4. The implementation of the WT calculation was greatly facilitated by the use of the open source python library PyWavelets.⁵⁸

2. Wavelet analysis of the discharge

The WT of the time series of the discharge current, the capacitive signal, and the ionic current have been calculated and give very similar spectrograms. Indeed, the variations in these signals are highly correlated, especially for fast oscillations, as can be seen in Fig. 12, where the coherence of the discharge current and the capacitive signal is plotted. The coherence of two signals is the normalized cross spectral density. It is a statistic that can be used to examine the relationship between two signals for given frequency components. Here, in the graph in

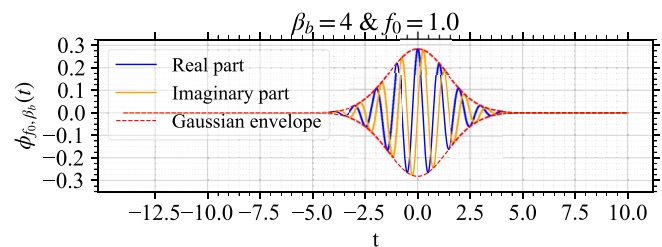


FIG. 11. Complex Morlet wavelet function illustration.

Fig. 12, we see that oscillations with frequencies between 30 and 130 kHz are well correlated. The only visible differences between the discharge current and capacitive signal series are in the distribution of the power spectral density: like in the Fourier spectra, the BM oscillation concentrates the power spectral density (PSD) in the frequency space of the discharge current, making the other oscillations less visible. On the other hand, the relative weight of the fast and BM oscillations is more balanced on the capacitive signal, which means that the fast oscillations can be investigated in greater detail.

By studying the graphs in Fig. 6, we can see that there is an anti-correlation between the fast oscillations on the discharge current peaks (in blue) and the capacitive voltage peaks (in green) occurring at frequencies between a few tens and a few hundreds of kilohertz. As soon as a pulse is detected by the capacitive antenna, the discharge current starts to increase. As the antenna is located outside the enclosure, a change in its potential means either a change in an electric field and/or in the plasma potential, which tells us about a charge displacement or a reorganization of the plasma propagating into the plume. Disturbances in the plasma potential over a frequency range ranging from 60 to 150 kHz can suggest the presence of ion transit time oscillations.

Since these two signals are correlated in this frequency range, we will illustrate our observations here with wavelet spectrograms calculated from series of the capacitive signal. They have been plotted in Fig. 13.

Let us look first at the low discharge voltage regimes (A). Starting with the lowest frequencies, we find an initial bright red band that is continuous throughout the spectrum, around 4 kHz for $U_d = 115$ V (A1) and 7 kHz for $U_d = 125$ V (A2) marking the fundamental frequency of the BM. The Fourier spectra are also shown in the panels on the left of the graphs in burgundy red, showing the BM at the same frequency. The frequency band appears wider on the wavelet spectrum than on the Fourier spectrum, because in frequency space, the complex Morlet wavelet function is defined as a Gaussian of non-zero width. This width is a function of the probed frequency and can be seen as an analogy to Heisenberg's uncertainty principle: in time-frequency analysis, we cannot have perfect resolution in both time and frequency space. In this regime we can see that the BM frequency is not stabilized through time: it oscillates by a few kHz during the probed time interval. This is particularly noticeable in the A1 regime, where the period of BM oscillations can vary by several hundreds of μ s, and these variations were also observed in the discharge current in Fig. 6. A period of the BM is bordered by the two dashed lines. When U_d increases, the BM frequency tends to stabilize, approaching a straight line on the

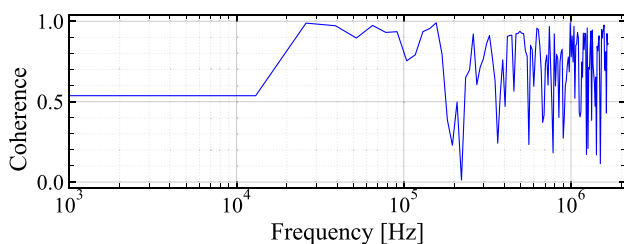


FIG. 12. Coherence of discharge current and capacitive signal as a function of oscillation frequency; calculated using matplotlib cohere function with a resampling frequency of 3.3 MHz.

spectrogram. As we move up toward higher frequencies, we encounter bands corresponding to the harmonics of the BM. Depending on the oscillation regime, between 2 and 5 harmonics bands can be easily be observed on the spectrogram. By raising the frequency further, between 30 and 200 kHz, we see discontinuous colored areas, in phase with the areas where rapid oscillations occur when the maximum discharge current is reached, which confirms the intermittent nature of these oscillations. The dotted lines show the development zone for the rapid oscillations on the discharge current. A quick comparison with the Fourier spectrum immediately reveals the power of the WT: where these oscillations form a small and broadened bump on the Fourier spectrum, very distinct islets appear on the WT. This reveals that there are several types of rapid oscillation that can be divided into two blocks of frequencies, the first oscillating between 20 and 90 kHz and the second between 100 and 350 kHz. In regime A, we can see that the frequencies of the rapid oscillations are not constant over time and that they change as the BM cycle progresses. In the unstable regime A1, the frequency variations seem quite random, although we can guess an increase and then a decrease in the frequency of oscillations evolving between 20 and 90 kHz within certain BM oscillations (such as between 0 and 600 μ s). If the oscillations of the lower frequency block occur continuously during the discharge, the oscillations of the upper block occur essentially when the discharge current is at its maximum. In the A2 regime, where the BM oscillations are more stable, we can clearly see a gradual increase in the frequency of the oscillations, which tends to create a frequency continuity between the two previously identified blocks. This frequency shift begins when the discharge current is still minimal and ends when the discharge current has fallen sharply. We can, therefore, assume that the phenomena at work in these oscillations are active in the ionization zone, which, as we recall, is strongly impacted by the BM.

Above 700 kHz and up to MHz, flame-like oscillations can be seen on the spectrogram. The apparition of these oscillations is synchronized with the reaching of the maximum of the picked up capacitive signal, which corresponds to the rise in the discharge current due to the fast oscillations previously defined. On the spectrograms, these time instants are indicated by dotted lines. They then disappear during the descending phase of the ITTO oscillations. Note that our Shannon–Nyquist cut-off frequency is 25 MHz, so there are no effects due to the signal sampling. Finally, we find oscillations displaying a similar behavior around 400 kHz when the discharge current is minimal between two BM oscillations.

To summarize, in the A regime, there are at least three levels of instability between kilohertz and megahertz. These oscillations appear intermingled with each other. We observed that when BM oscillations are unstable (in frequency and in shape), ITTO oscillations are also very unstable and evolve chaotically over time on a BM cycle. In contrast, in the A2 regime, when BM oscillations stabilize and become more regular, the evolution of the ITTO frequency is also more regular, with a frequency shift toward the higher frequencies over time during a BM cycle. We can, therefore, assume that instabilities at lower frequencies periodically create favorable conditions for the emergence of oscillations at higher frequencies.

By increasing the discharge voltage, we enter the high-amplitude BM oscillation regime (B), and we can see that the band corresponding to the BM increases in frequency, which was already highlighted on the spectrogram in Fig. 7. We can also remark that unlike regime A, in

this regime the BM oscillations are very regular, which is reflected in the straightness of the BM bands. With the increase in the discharge voltage, we can also see on the spectrograms that 20–90 kHz band gives up its place to the bands corresponding to the BM harmonics. However, in the B1 regime, on certain BM oscillations, there are still zones in this frequency band where the spectral power is higher (such as between 70 and 100 μs on the spectrogram at 215 V). Only oscillations with a frequency between 100 and 300 kHz remain. There is also

a noticeable change in the behavior of these fast oscillations, which are now perfectly localized when the discharge current is maximum and their central frequency is fixed. It can be observed that the central frequency of these oscillations is juxtaposed with that of one of the harmonics of the BM, located between the 4th and 6th harmonics. Oscillations are no longer found in regimes of low discharge current, which may be too low to maintain the plasma discharge and the richness of its dynamics.

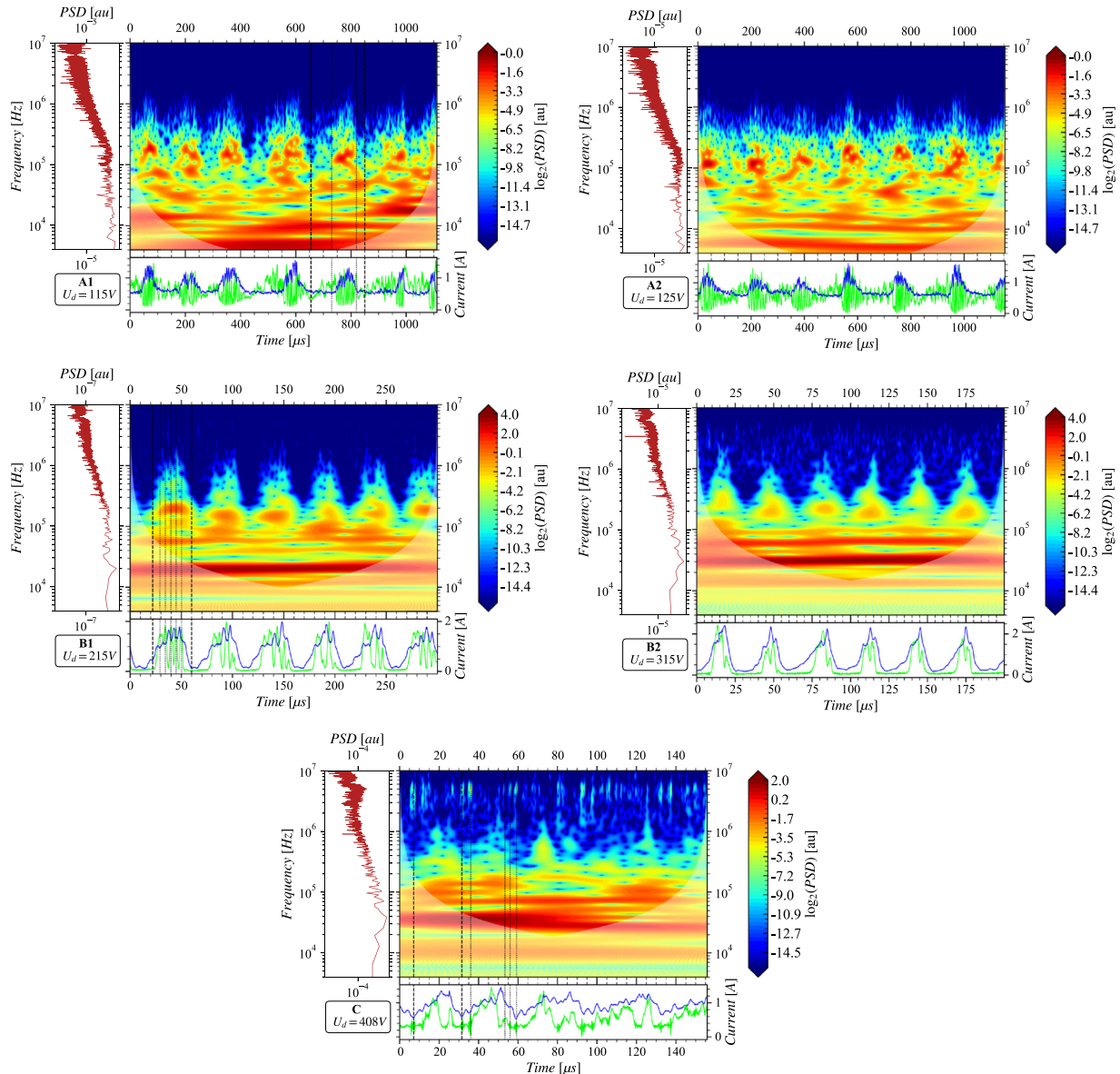


FIG. 13. Wavelet spectrograms for each of the observed regimes. The central zone is the spectrogram of a time segment of the chosen time series: the x-axis represents time and the y-axis represents frequency. The color scale is logarithmic and represents the PSD. The white transparent area is the coherence cone; its border marks the area in which the coherence of the WT can be reduced due to edge effects. The red curve on the left is the Fourier spectrum corresponding to the entire time series. The lower graph contains the curves associated with the discharge current (blue) and the capacitive signal in arbitrary units (green).

Green peaks can also be seen on the spectrograms at frequencies between 300 and 700 kHz. These peaks are visible at the local maximum of the discharge current during oscillations at around 100 kHz. By probing higher frequencies, oscillations can still be observed between 0.7 and 1.1 MHz. These follow the same dynamics as in regime A. In case B1 where several oscillations are superimposed on the BM, a PSD peak is observed when the capacitive signal is locally maximum during the oscillations at around 100 kHz. At higher frequencies, such as the frequency band between 2 and 10 MHz, oscillation packets gradually appear as U_d increase. At this point, these oscillations seem too random in both time and frequency and have too low a PSD for us to consider them significant compared to the ambient EM noise.

To sum up, in regime B, the oscillations become more regular, whether it is the BM whose frequency and amplitudes are more stable or the oscillations in the hundreds of kilohertz whose central frequency no longer evolves and overlaps with the frequency of some of the harmonics of the BM. It could be imagined that an interaction between the BM and the fast oscillations via the BM harmonics is helping to stabilize these fast oscillations. In addition, it should be remembered that in this regime the amplitude of the discharge current oscillations doubles, so it could be suggested that there might be some resonance interactions between the two oscillations. Finally, at higher frequencies, oscillations appear temporarily when the local maxima of the discharge current and capacitive signal oscillations are reached.

Finally, in regime C (and as the last cases), we used as an example a discharge voltage of 408 V, we still see oscillations, such as the BM, around 14 kHz, and the fast oscillations, between 100 and 400 kHz. However, these oscillations have become unstable, both from a frequency point of view, with the broadening of the frequency bands, and from a time point of view, with different oscillation modes alternating. When the amplitude of the BM is low, between 60 and 100 μs for example, the rapid oscillations are more regular and their frequency is more prominent, which is reflected in the thinness of the corresponding band on the spectrogram at 100 kHz. Finally, between 3 and 7 MHz, we observe oscillation packets that are synchronized with the local minima of the discharge current during oscillations at 120 kHz and corresponding to a reception of a wave packet on the capacitive antenna (examples are shown on the spectrogram with the location of the thin dotted black bars). We can also see that these MHz oscillations are more visible because their PSD is greater when the discharge current reaches the minimum of the BM. On the other hand, these MHz oscillations are much more visible on the spectrograms of the capacitive signal and the ion current than on the discharge current, where they can only be seen as a trace. This could, therefore, be an instability affecting the movement of the ions. We, therefore, need to study the characteristics of the ions in more details.

3. Ion wavelet analysis

In parallel with the time measurements of the discharge current, the capacitive signal, the coupling potential of the cathode with the ground, and the ion current were also recorded. These were made using the RPA placed in the central axis of the thruster with the ion filter grid set to being unbiased, so that the RPA no longer made any selection on the energy of the ions collected, giving us a view of the variation of the ion current. The spectrograms shown in Fig. 14 are taken from the ion current time series for a xenon flow rate of 0.6 mg/s.

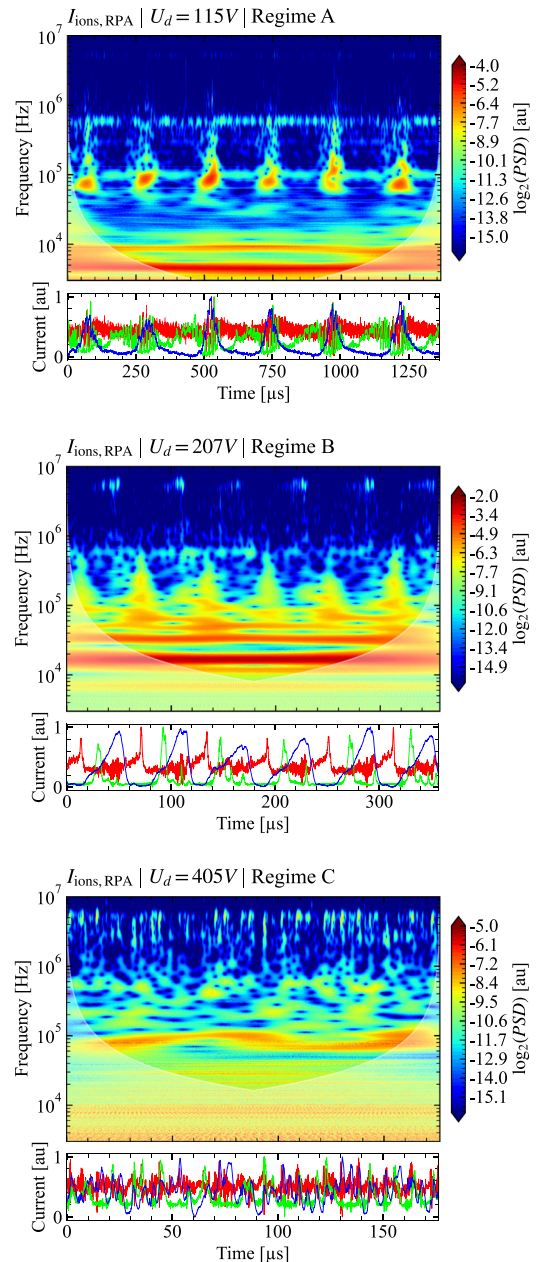


FIG. 14. Wavelet spectrogram of time series of the total ion current collected with a RPA for a gas flow rate of 0.6 mg/s and from the top to the bottom, a discharge voltage of 115, 207, and 405 V. The lower graphs plot the discharge currents (in blue), the ion currents (in red, collected at the RPA) and the capacitive signal (in green) on a common time base with the spectrograms.

The spectrograms in Fig. 14 show several frequency bands. The first band, which is more or less pronounced in each of the spectrograms, is located between 4 and 6 MHz, and we note that the frequency of these oscillations may correspond to the plasma pulsation of the ions. At 115 V, in regime A, these oscillations are episodic, and we cannot really say whether they are anything other than ambient

electromagnetic noise. With the rise of the discharge voltage and the transition to regime B, we observe a succession of wave bursts whose intensity increases with time before gradually disappearing when the BM is restarted (when the discharge current increases). In regime C, the MHz oscillations are much more pronounced and there seem to be more occurrences when 500 kHz oscillations are present.

These oscillations around 500 kHz are also visible regardless of the discharge voltage. Depending on the oscillation regime, their location relative to other oscillations with longer periods seems to change. They are intermittent and relatively homogeneously distributed in regimes A and C, and appear to be activated when the capacitive voltage inflects. By contrast, in regime B, they seem to be located more often in the time interval corresponding to a low discharge current.

Finally, at lower frequencies, the oscillations are very similar to those already observed on the spectrograms of the discharge current and capacitive signal in Fig. 13. Particularly in regime A, between 60 and 110 kHz, we can clearly and distinctly see the islands of oscillations previously associated with ITTO when the discharge current is at its maximum. However, we note that there are still oscillations around 100 kHz, although their PSD and, therefore, their amplitude are relatively low. In regimes A and B, we can clearly see the continuous bands associated with BM oscillations around 5 kHz. In regime C, where the BM is intermittent (on the spectrogram shown here, the BM is not present), we mainly observe the fast ITTO oscillations between 80 and 100 kHz and we note that their frequency is not very stable and depends on the value of the discharge current.

To summarize, the ion current also displays the marks of numerous instabilities, including the signatures of the BM and ITTO, but also other oscillations that we have not been identified, some of which appear to be interdependent or at least dependent on the conditions created on larger scales by the instabilities with longer periods. We also note that the oscillations around 500 kHz and 4–6 MHz become more pronounced as the discharge voltage increases. This suggests the presence of different physical phenomena, which are more pronounced when the discharge current is low, and which act mainly on the current collected by the RPA. We cannot exclude the possibility that at least one of these oscillations develops because of plasma instability inside the RPA or is a capacitive signal picked up by the RPA and/or on its wires inside the plasma (the noise-to-signal ratio was evaluated at 6% by comparing the signals collected by the RPA in the plasma with and without a shield in front of the instrument entrance, for a constant discharge voltage and flow rate). The oscillations present in 4–6 MHz frequency range are also observable on the spectrogram of the capacitive signal (and discharge current) at high voltage in Fig. 13 (for $U_d = 408$ V). In the article,⁵⁹ a similar signature of oscillations was observed on the Fourier spectrum of the discharge current and were attributed to electron-drift type oscillations.

IV. CONCLUSION

The study of the discharge current oscillations enabled us to identify several oscillation regimes in which several types of oscillations coexist for different times, frequencies, and amplitudes. It was shown that in each of the oscillation regimes, the ion distribution functions were affected in different ways. We were also able to demonstrate a correlation between the discharge current oscillations and the variation in a capacitive signal collected outside the chamber.

The diagnostic tool of time-frequency analysis by wavelet transform has been imported into the field of the study of propulsion plasma

oscillations, and some interesting results have been obtained. The advantage of this technique over analyses based on the Fourier transform is its relative indifference to the fact that our signals are often irregular and that some oscillations are intermittent. We can, therefore, capture intermittent oscillating structures, such as certain oscillations that only appear at certain precise moments in relation to another oscillation. It has, therefore, revealed the coexistence and interdependence of several different instabilities: the BM, the ITTO, oscillations at higher frequencies ranging from several hundred kilohertz to megahertz and a RS in the azimuthal direction. We suspect a possible interaction between the breathing mode and the higher-frequency oscillations leading to ITTO. It was observed that a transition between two different oscillations regime seemed to occur when the frequency of one of the BM harmonics became a multiple of the frequency of the higher-frequency oscillations, in parallel with a doubling of the discharge current and a deformation of the IDFs. In all oscillation regimes, when the discharge current varied quickly inside a BM cycle, a pulse is detected on the capacitive signal, reflecting the variation of an electric field in the plasma. These capacitive signal peaks are also correlated with the ITTO oscillations on the discharge current, which they precede. All this information highlights the instability of ITTO. Rapid oscillations were also observed at low discharge voltages, but without any asymmetric change in the IDF, which raises the question of the existence of different ITTO excitation modes. It was also shown that at low discharge voltage, the ITTO center frequency was not fixed in time but shifted toward higher frequencies as the BM advanced (in regime A).

However, we did not identify the mechanism responsible for triggering ITTO. Fluctuations on the cathode potential have been measured in the same frequency ranges, but given that the cathode plasma can exhibit oscillation modes over this same frequency range, it is not currently possible to know whether there is a causal link between these oscillations. We observe that the conditions necessary for rapid oscillations are met when ionization is at its maximum and no longer evolves with U_d , the azimuthal electron current could also be destabilized by an increasing electron current coming from the cathode and leading to the formation of ITTO. By increasing the discharge voltage (>300 V), the electron current passing through the barrier increases and at the same time we observe a reduction in the rate of presence and amplitude of BM oscillations to the benefit of fast oscillations. In this regime, the average energy of the ions is always close to the energy supplied to the discharge. So, instability combinations may increase the anomalous transport.

It was observed that oscillations at MHz are also much more visible on the ion currents captured by the RPA (without polarization of the filter grid), than on the other signals. So, they might be oscillations developing in the plasma plume and not in the thruster channel (to be confirmed). Additionally, these oscillations are essentially present when the discharge current is low between two BM cycles or in regimes where the BM is intermittent. The triggering mechanisms are, therefore, probably different from those responsible for oscillations at lower frequencies.

Questions remain about the mechanisms for stabilizing the oscillations corresponding to ITTOs in regime B and about the possible coupling of instabilities on different scales, leading to a doubling of discharge current amplitudes. There are also questions about the origin of the MHz oscillations visible in the ion current collected by the RPA (without ion filtering) and about their temporal dependence on oscillations with longer periods.

It would also be interesting to determine the temporal evolution of the electron current flowing through the magnetic barrier to determine the impact of low-frequency oscillations on anomalous transport. This work is in progress.

ACKNOWLEDGMENTS

Q.D.D. has benefited from a Ph.D. funding from the French Ministry of Research. This work was supported by the CNES agency. This work has been carried out within the framework of the EUROfusion Consortium, funded by the European Union via the Euratom Research and Training Programme (Grant Agreement No 101052200—EUROfusion). Views and opinions expressed are however those of the author(s) only and do not necessarily reflect those of the European Union or the European Commission. Neither the European Union nor the European Commission can be held responsible for them. Q.D.D. also likes to thank Mr. J. Stevens for his suggestions to improve the quality of the English of this manuscript.

AUTHOR DECLARATIONS

Conflict of Interest

The authors have no conflicts to disclose.

Author Contributions

Quentin Delavière—Delion: Conceptualization (equal); Data curation (equal); Formal analysis (equal); Investigation (equal); Methodology (equal); Visualization (equal); Writing—original draft (equal); Writing—review & editing (equal). **Freddy Gaboriau:** Formal analysis (equal); Funding acquisition (equal); Project administration (equal); Resources (equal); Supervision (equal); Validation (equal); Writing—review & editing (equal). **Gwenaél Fubiani:** Conceptualization (equal); Formal analysis (equal); Funding acquisition (equal); Project administration (equal); Supervision (equal); Writing—review & editing (equal). **Laurent Garrigues:** Formal analysis (equal); Writing—review & editing (equal).

DATA AVAILABILITY

The data that support the findings of this study are available from the corresponding author upon reasonable request.

REFERENCES

- A. I. Morozov, “The conceptual development of stationary plasma thrusters,” *Plasma Phys. Rep.* **29**(3), 235–250 (2003).
- D. Lev, R. M. Myers, K. M. Lemmer, J. Kolbeck, H. Koizumi, and K. Polzin, “The technological and commercial expansion of electric propulsion,” *Acta Astronaut.* **159**, 213–227 (2019).
- S. Mazouffre, “Electric propulsion for satellites and spacecraft: Established technologies and novel approaches,” *Plasma Sources Sci. Technol.* **25**(3), 033002 (2016).
- D. Krejci and P. Lozano, “Space propulsion technology for small spacecraft,” *Proc. IEEE* **106**(3), 362–378 (2018).
- N. Brown and M. L. R. Walker, “Review of plasma-induced Hall thruster erosion,” *MDPI* **10**, 3775 (2020).
- E. Y. Choueiri, “Plasma oscillations in Hall thrusters,” *Phys. Plasmas* **8**(4), 1411 (2001).
- V. Mazières, F. Gaboriau, A. Guglielmi, V. Laquerbe, R. Pascaud, and O. Pascal, “Broadband (kHz–GHz) characterization of instabilities in Hall thruster inside a metallic vacuum chamber,” *Phys. Plasmas* **29**(7), 072107 (2022).
- S. Tsikata, A. Héron, and C. Honoré, “Hall thruster microturbulence under conditions of modified electron wall emission,” *Phys. Plasmas* **24**(5), 053519 (2017).
- N. Yamamoto, N. Kuwabara, D. Kuwahara, S. Cho, Y. Kosuga, and G. D. Pradalier, “Observation of plasma turbulence in a Hall thruster using microwave interferometry,” *J. Propul. Power* **39**(6), 849–855 (2023).
- A. Guglielmi, “Propulseur à courant de Hall double étage à source RF inductive: étude expérimentale du fonctionnement et des instabilités basses fréquences,” Ph.D. thesis, Paul Sabatier, Toulouse, 2020.
- E. Chesta, C. M. Lam, N. B. Meezan, D. P. Schmidt, and M. A. Cappelli, “A characterization of plasma fluctuations within a Hall discharge,” *IEEE Trans. Plasma Sci.* **29**(4), 582–591 (2001).
- J. Kurzyna, S. Mazouffre, A. Lazurenko, L. Albarède, G. Bonhomme, K. Makowski, M. Dudeck, and Z. Peradzyński, “Spectral analysis of Hall-effect thruster plasma oscillations based on the empirical mode decomposition,” *Phys. Plasmas* **12**(12), 123506 (2005).
- L.-Q. Wei, L. Han, D.-R. Yu, and N. Guo, “Low-frequency oscillations in Hall thrusters,” *Chin. Phys. B* **24**(5), 055201 (2015).
- K. Hara, S. Keller, and Y. Raitses, “Measurements and theory of driven breathing oscillations in a Hall effect thruster,” AIAA Paper No. 2016-4532, 2016.
- A. Guglielmi, A. M. Ortega, F. Gaboriau, and J.-P. Boeuf, “Influence of double-stage operation on breathing oscillations and rotating spokes in the ID-HALL thruster,” in 36th International Electric Propulsion Conference, University of Vienna, Vienne, Autriche, 2019.
- A. Martín Ortega, A. Guglielmi, F. Gaboriau, C. Boniface, and J. P. Boeuf, “Experimental characterization of ID-Hall, a double stage Hall thruster with an inductive ionization stage,” *Phys. Plasmas* **27**(2), 023518 (2020).
- V. Giannetti, M. M. Saravia, and T. Andreussi, “Measurement of the breathing mode oscillations in Hall thruster plasmas with a fast-diving triple Langmuir probe,” *Phys. Plasmas* **27**(12), 123502 (2020).
- M. Baird, T. Kerber, R. McGee-Sinclair, and K. Lemmer, “Plume divergence and discharge oscillations of an accessible low-power Hall effect thruster,” *Appl. Sci.* **11**(4), 1973 (2021).
- M. J. Sekerak, A. D. Gallimore, D. L. Brown, R. R. Hofer, and J. E. Polk, “mode transitions in Hall-effect thrusters induced by variable magnetic field strength,” *J. Propul. Power* **32**(4), 903–917 (2016).
- N. Gascon, M. Dudeck, and S. Barral, “Wall material effects in stationary plasma thrusters. I. Parametric studies of an SPT-100,” *Phys. Plasmas* **10**(10), 4123–4136 (2003).
- J. Bareilles, G. J. M. Hagelaar, L. Garrigues, C. Boniface, J. P. Boeuf, and N. Gascon, “Critical assessment of a two-dimensional hybrid Hall thruster model: Comparisons with experiments,” *Phys. Plasmas* **11**(6), 3035–3046 (2004).
- J. P. Boeuf and L. Garrigues, “Low frequency oscillations in a stationary plasma thruster,” *J. Appl. Phys.* **84**(7), 3541–3554 (1998).
- T. Lafleur, P. Chabert, and A. Bourdon, “The origin of the breathing mode in Hall thrusters and its stabilization,” *J. Appl. Phys.* **130**(5), 053305 (2021).
- O. Chapurin, A. Smolyakov, G. Hagelaar, J.-P. Boeuf, and Y. Raitses, “Fluid and hybrid simulations of the ionization instabilities in Hall thruster,” *J. Appl. Phys.* **132**(5), 053301 (2022).
- J. Vaudolon and S. Mazouffre, “Observation of high-frequency ion instabilities in a cross-field plasma,” *Plasma Sources Sci. Technol.* **24**(3), 032003 (2015).
- J. Vaudolon, “Electric field determination and magnetic topology optimization in Hall thruster,” Ph.D. thesis, ICARE—Institut de Combustion, Aérothermique, Réactivité et Environnement, Orléans, 2015.
- G. J. M. Hagelaar, J. Bareilles, L. Garrigues, and J.-P. Boeuf, “Two-dimensional model of a stationary plasma thruster,” *J. Appl. Phys.* **91**(9), 5592–5598 (2002).
- F. Petronio, “Plasma instabilities in Hall Thrusters: A theoretical and numerical study,” Ph.D. thesis, École Polytechnique, Palaiseau, 2023.
- Y. B. Esipchuk, A. I. Morozov, and T. Trofimov, “Plasma oscillations in closed-drift accelerator with an extended acceleration zone,” *Sov. Phys. Tech. Phys.* **18**(7), 928–932 (1973).
- S. Tsikata, “Small-scale electron density fluctuations in the Hall thruster, investigated by collective light scattering,” Ph.D. thesis, École Polytechnique, Palaiseau, 2009.
- T. Dubois, L. Garrigues, S. Tsikata, and M. Chung To Sang, “Insights into Hall thruster radial physics via incoherent Thomson scattering,” in 37th International Electric Propulsion Conference Massachusetts Institute of Technology, Boston, MA, USA, 2022.

- ³²G. S. Janes and R. S. Lowder, "Anomalous electron diffusion and ion acceleration in a low-density plasma," *Phys. Fluids* **9**(6), 1115–1123 (1966).
- ³³M. S. McDonald and A. D. Gallimore, "Rotating spoke instabilities in Hall thrusters," *IEEE Trans. Plasma Sci.* **39**(11), 2952–2953 (2011).
- ³⁴C. L. Ellison, Y. Raitses, and N. J. Fisch, "Cross-field electron transport induced by a rotating spoke in a cylindrical Hall thruster," *Phys. Plasmas* **19**(1), 013503 (2012).
- ³⁵S. Mazouffre, L. Grimaud, S. Tsikata, K. Matyash, and R. Schneider, "Rotating spoke instabilities in a wall-less Hall thruster: Experiments," *Plasma Sources Sci. Technol.* **28**(5), 054002 (2019).
- ³⁶A. Guglielmi, F. Gaboriau, and J. P. Boeuf, "Simultaneous measurements of axial motion and azimuthal rotation of non-uniformities ("spokes") in a Hall thruster," *Phys. Plasmas* **29**(11), 112108 (2022).
- ³⁷J. M. Sequeira Mealha and B. Senart, "Experimental characterization of the double stage Hall thruster ID-Hall by retarding potential analyzer," Master thesis, Laplace, Toulouse, 2019.
- ³⁸A. Smirnov, Y. Raitses, and N. J. Fisch, "Experimental and theoretical studies of cylindrical Hall thrusters," *Phys. Plasmas* **14**(5), 057106 (2007).
- ³⁹Y. Raitses, A. Smirnov, and N. J. Fisch, "Enhanced performance of cylindrical Hall thrusters," *Appl. Phys. Lett.* **90**, 221502 (2007).
- ⁴⁰A. Loyan, F. Darnon, L. Albarede, V. Lago, P. Lasgorceix, and M. Dudeck, "Correlation between hollow cathode operating conditions and Hall thruster (SPT100-ML) performance characteristics," AIAA Paper No. 2002-4101, 2002.
- ⁴¹H. Valentin and M. Stéphane, "Optimization of a Faraday cup collimator for electric propulsion device beam study: Case of a Hall thruster," *Appl. Sci.* **11**(5), 2419 (2021).
- ⁴²C. P. Kadlec, "Caractérisations spatio-temporelles de jets ioniques: développement des diagnostics et application a la propulsion ionique," Ph.D. thesis, GREMI, Orléans, 1998.
- ⁴³H. Andrei, V. Covlea, V. V. Covlea, and E. Barna, "The smoothing and the digital processing of Langmuir probe characteristic," *Rom. J. Phys.* **55**(2), 51–56 (2003).
- ⁴⁴A. Caldarelli, F. Filleul, R. W. Boswell, C. Charles, N. J. Rattenbury, and J. E. Cater, "Data processing techniques for ion and electron-energy distribution functions," *Phys. Plasmas* **30**(4), 040501 (2023).
- ⁴⁵J. Vaudolon, D. Harribey, C. Henaux, S. Mazouffre, and A. Rossi, "Influence de la topologie magnétique et des conditions expérimentales sur les performances du propulseur PPS-FLEX," Unpublished Report RAPPORT PE-R-02–2014, CNRS, CNES, Safran, ICARE, Orléans, 2014.
- ⁴⁶B. K. Parida, K. P. Sooraj, S. Hans, V. Pachchigar, S. Augustine, T. Remyamol, M. R. Ajith, and M. Ranjan, "Sputtering yield and nanopattern formation study of BNSiO₂ (Borosil) at elevated temperature relevance to Hall Effect Thruster," *Nucl. Inst. Methods Phys. Res., B* **514**, 1–7 (2022).
- ⁴⁷B. P. Van Milligen, C. Hidalgo, and E. Sánchez, "Nonlinear phenomena and intermittency in plasma turbulence," *Phys. Rev. Lett.* **74**(3), 395–398 (1995).
- ⁴⁸M. McDonald, R. Liang, and A. D. Gallimore, "Practical application of wide bandwidth floating emissive probes and wavelet analysis to the X2 nested Hall thruster," in 33rd International Electric Propulsion Conference, Washington D. C., USA, 2013.
- ⁴⁹G. Bonhomme, N. Lemoine, F. Brochard, A. Lazurenko, S. Mazouffre, and M. Dudeck, "Characterization of high frequency plasma oscillations in a Hall effect thruster," in 30th International Electric Propulsion Conference, Florence, Italia, 2007.
- ⁵⁰M. S. McDonald, M. J. Sekerak, A. D. Gallimore, and R. R. Hofer, "Plasma oscillation effects on nested Hall thruster operation and stability," in 2013 *IEEE Aerospace Conference, Big Sky, MT* (IEEE, 2013), pp. 1–12.
- ⁵¹C. Torrence and G. P. Compo, "A practical guide to wavelet analysis," *Bull. Amer. Meteor. Soc.* **79**(1), 61–78 (1998).
- ⁵²M. Farge, K. Schneider, and P. Devynck, "Analyse en ondelettes de signaux de plasmas de bord, et extraction des événements cohérents," CEA, Contrat CEA/EURATOM Rapport final, 1ère année, 2001. See <http://wavelets.ens.fr/PUBLICATIONS/ARTICLES/PDF/156.pdf>.
- ⁵³Y. Meyer, S. Jaffard, and O. Rioul, "L'analyse par ondelettes," *Pour la Sci.* **1987**, 28–37.
- ⁵⁴J.-Y. Richard, "Présentation de la méthode des Ondelettes," Observatoire de Paris, 2006. See https://www5.obs-mip.fr/wp-content-omp/uploads/sites/28/2017/11/Ondelettes_GRGs_2006.pdf.
- ⁵⁵A. Bultheel, "Learning to swim in a sea of wavelets," *Bull. Belg. Math. Soc.* **2**(1), 1–46 (1995).
- ⁵⁶M. Farge, "Wavelet transforms and their applications to turbulence," *Annu. Rev. Fluid Mech.* **24**, 395–458 (1992).
- ⁵⁷D. B. Percival and A. T. Walden, *Wavelet Methods For Time Series Analysis*, Cambridge Series in Statistical and Probabilistic Mathematics (Cambridge University Press, Cambridge, 2000).
- ⁵⁸F. Malgouyres, "Analyse par ondelettes," Master 2 IMAT Mathematical Engineering Course in Toulouse (in French). See <http://www.math.univ-toulouse.fr/~fimalgouy/enseignement/ondelettes.html>.
- ⁵⁹N. Kuwabara, M. Chono, T. Morita, and N. Yamamoto, "Anomalous electron transport in hall thrusters: Electric field fluctuation measurement," *Aerosp. Technol. Jpn.* **19**(1), 81–86 (2021).